



HAL
open science

Martian electron foreshock from MAVEN observations

K. Meziane, C. X. Mazelle, N. Romanelli, D. L. Mitchell, J. R. Espley, J. E. P. Connerney, A. M. Hamza, J. Halekas, J. P. Mcfadden, B. M. Jakosky

► To cite this version:

K. Meziane, C. X. Mazelle, N. Romanelli, D. L. Mitchell, J. R. Espley, et al.. Martian electron foreshock from MAVEN observations. *Journal of Geophysical Research Space Physics*, 2017, 122, pp.1531-1541. 10.1002/2016JA023282 . insu-03677079

HAL Id: insu-03677079

<https://insu.hal.science/insu-03677079>

Submitted on 25 May 2022

HAL is a multi-disciplinary open access archive for the deposit and dissemination of scientific research documents, whether they are published or not. The documents may come from teaching and research institutions in France or abroad, or from public or private research centers.

L'archive ouverte pluridisciplinaire **HAL**, est destinée au dépôt et à la diffusion de documents scientifiques de niveau recherche, publiés ou non, émanant des établissements d'enseignement et de recherche français ou étrangers, des laboratoires publics ou privés.

Copyright

RESEARCH ARTICLE

10.1002/2016JA023282

Special Section:

Major Results From the MAVEN Mission to Mars

Key Points:

- Two types of energetic electron populations are present upstream of the Martian bow shock
- Energetic electrons emanate from the entire bow shock surface of Mars
- Similar and distinct features between the terrestrial and Martian foreshocks are identified

Correspondence to:

K. Meziane,
karim@unb.ca

Citation:

Meziane, K., C. X. Mazelle, N. Romanelli, D. L. Mitchell, J. R. Espley, J. E. P. Connerney, A. M. Hamza, J. Halekas, J. P. McFadden, and B. M. Jakosky (2017), Martian electron foreshock from MAVEN observations, *J. Geophys. Res. Space Physics*, 122, 1531–1541, doi:10.1002/2016JA023282.

Received 4 AUG 2016

Accepted 12 DEC 2016

Accepted article online 27 JAN 2017

Published online 2 FEB 2017

Martian electron foreshock from MAVEN observations

K. Meziane¹ , C. X. Mazelle² , N. Romanelli² , D. L. Mitchell³ , J. R. Espley⁴ , J. E. P. Connerney⁴, A. M. Hamza¹, J. Halekas⁵ , J. P. McFadden³, and B. M. Jakosky⁶ 

¹Department of Physics, University of New Brunswick, Fredericton, New Brunswick, Canada, ²IRAP, Université Paul Sabatier/CNRS, Toulouse, France, ³Space Sciences Laboratory, University of California, Berkeley, USA, ⁴NASA Goddard Space Center, Greenbelt, Maryland, USA, ⁵Department of Physics and Astronomy, University of Iowa, Iowa City, Iowa, USA, ⁶Laboratory for Atmospheric and Space Physics, University of Colorado Boulder, Boulder, Colorado, USA

Abstract Flux enhancements of energetic electrons are always observed when the Mars Atmosphere and Volatile Evolution (MAVEN) spacecraft is magnetically connected to the shock. The observations indicate that the foreshock electrons consist of two populations. The most energetic ($E \geq 237$ eV) originate from a narrow region at the nearly perpendicular shock. They always appear as spikes, and their flux level reaches a maximum when the angle θ_{Bn} approaches 90° . The other population emanates from the entire Martian bow shock surface, and the flux level decreases slightly from the quasi-parallel to quasi-perpendicular regions. A detailed examination of the pitch angle distribution shows that the enhanced fluxes are associated with electrons moving sunward. Annulus centered along the interplanetary magnetic field direction is the most stringent feature of the 3-D angular distribution. The gyrotropic character is observed over the whole range of shock geometry. Although such signatures in the electron pitch angle distribution strongly suggest that the reflection off the shock of a fraction of the solar wind electrons is the main mechanism for the production of Martian foreshock electrons, the decay of the flux of the second population on the other hand has yet to be understood.

1. Introduction

The existence of planetary bow shocks has been predicted by *Axford* [1962] and *Kellogg* [1962], whose original work focused on the supersonic nature of the solar wind and its consequences. These standing plasma shock structures result from the interaction of the solar wind flow with the planet's environment. In the case of Mars, the Mars Global Surveyor (MGS) mission established an upper threshold of 0.5 nT of the Mars global magnetic field [*Acuña et al.*, 1998]. Despite its weak gravity, the red planet is not devoid of an atmosphere, in which the upper layers are continuously exposed to ionization due to solar radiation. As a consequence, and because of their electric conductivity, the upper layers on the dayside prevent the direct impact of the solar wind plasma with the surface of the planet. The presence of this obstacle immersed in the supersonic-super-Alfvénic solar wind plasma induces the formation of a shock upfront whose nose is located at $\sim 1.5 R_M$ (Mars radius) from the center of the planet. Early space missions to Mars, including Mars 3 and 5, Mariner-4 and Phobos-2, as well as the most recent ones, MGS and Mars Express (MEX), have all confirmed the existence of a bow shock. Inbound and outbound shock crossings reveal magnetic field and plasma compression accompanied by a solar wind deceleration.

Like magnetized planets, the presence of the bow shock of Mars induces major upstream phenomena including foreshock formation. Subsequently, charged particle shock encounters, wave-particle interactions, and other nonlinear wave growth phenomena recurrently occur, providing a rich landscape of plasma physics processes. Because the Martian bow shock is immersed in an extended neutral exosphere [*Chaffin et al.*, 2015], specific processes take place on Mars that do not occur in the foreshock magnetized planets. A comprehensive overview on Mars foreshock phenomena can be found in *Mazelle et al.* [2004]. In the present report, the interaction of the solar wind electrons with the Martian bow shock is investigated.

Studies of Mars foreshock phenomena began with the Phobos-2 mission. Thermal and foreshock energetic electron measurements were first reported by *Skalsky et al.* [1993] using the HARP differential electrostatic analyzer Hyperbolic Retarding Potential differential electrostatic Analyzer (HARP) [*Kiraly et al.*, 1991]. The instrument consisted of two sensors disposed at 90° angle restricting the field of view (FOV) significantly.

A time window corresponding to the spacecraft spin period (~ 11 min) was needed to obtain a reasonable coverage in pitch angle; Phobos-2 spin axis was nearly parallel to the Sun direction. Moreover, although a full energy spectrum was obtained in a 27 s integration time, there was a gap of 56 s between successive measurements due to telemetry operation requirements. On a highly elliptical orbit reaching an apogee of $23.6 R_M$, the HARP electrostatic analyzer detected a spin-modulated electron flux in the 100–540 eV energy range. Using plasma waves as a proxy for a magnetic connection, *Skalsky et al.* [1993] noticed that significant electron fluxes were also seen when Phobos-2 did not appear to be magnetically connected to the shock. The electron flux reached a maximum only when the FOV and the magnetic field directions were nearly parallel. The authors interpreted these observations as a signature of the shock reflection of solar wind electrons. The spin-modulated electron flux events were seen for a period exceeding 1 h or more. Unless the interplanetary magnetic field (IMF) direction was observed to remain quasi-steady during this time period, Phobos-2 observations revealed that the source region of backstreaming electrons was quite large.

The previous studies on Martian foreshock electrons described above are essentially qualitative in nature, and the inherent interpretation is quite speculative. At this point, we believe that a quantitative analysis is suitable in order to comprehend the Martian electronic foreshock and the similarities that may exist with the terrestrial foreshock. Also, a precise determination of the source region is essential for a better understanding of the mechanism that produces the Martian foreshock electrons. Our goal is to carry this analysis out providing high bit rate telemetry data collected from a state of the art instrumentation including full field of view detectors. A study of this nature was not possible previously with Phobos-2 HARP data due to a poor time resolution and low count rates. In the next section, we briefly describe the Solar Wind Electron Analyzer (SWEA) experiment and the data collection. In section 3 the observations are presented. A quantitative analysis is developed in section 4. Finally, a concise conclusion is given in the last section.

2. MAVEN-SWEA Experiment

Since November 2015, MAVEN orbiter science operations have collected plasma and neutral particles in addition to magnetic field data. The most important goal of MAVEN mission is to understand the driving mechanism for the planet's atmosphere rarefying. With a highly elliptical path, the orbiter covers atmospheric layers located as low as ~ 150 km from the surface to the space region dominated by the solar wind plasma. When the apoapsis is located in the dayside, the spacecraft crosses the Martian bow shock twice per day, allowing a frequent coverage of the foreshock region. The MAVEN science payload consists of a Langmuir Probe, state of the art wave and particle instruments, an imaging UV spectrograph, and a magnetometer. In the present study, we will primarily focus on data collected by the SWEA detector and the magnetometer (MAG). Detailed information and science objectives can be found in *Jakosky et al.* [2015a, 2015b].

SWEA consists of a symmetrical hemispheric-shaped detector designed to measure electron flux with energies ranging from 3 eV to 4.6 keV. Within this energy range, SWEA is able to measure the solar wind velocity electron distribution as well as the suprathermal electrons present in the foreshock. The SWEA detector features an energy resolution of $\Delta E/E \sim 0.17$ and a field of view that spans 80% of all sky with an angular resolution of $\sim 20^\circ$; a full velocity distribution is obtained every 2 s. A complete description of this instrument can be found in *Mitchell et al.* [2015]. Solar wind measurements are also used in our study; these are obtained from the Solar Wind Ion Analyzer (SWIA), a toroidal energy detector with electrostatic deflectors [*Halekas et al.*, 2015]. Finally, MAVEN-MAG provides vectorial magnetic field measurements. The MAG sensors are placed at the ends of the MAVEN spacecraft solar panels. Because the magnetic field intensity may reach extremely small values in some regions of the Martian environment, spacecraft-induced magnetic fields as well as any noise erupting from various operation maneuvers or transient events are robustly estimated to obtain reliable physical measurements. Both static and spacecraft magnetic field offsets are monitored using spacecraft roll maneuvers [*Connerney et al.*, 2015] and high-precision measurements (on the order of ~ 0.35 nT or better). In terms of time resolution, MAG provides in the maximum high-telemetry mode 32 vectors per second. This rate is judged sufficient to study the dominant ion-scale plasma processes occurring at the bow shock or on Martian foreshock.

3. Observations

Although the present study is based on the analysis of one single time interval, the results provide, nevertheless, an important aspect of the Martian foreshock. Numerous SWEA electron energy spectrograms collected

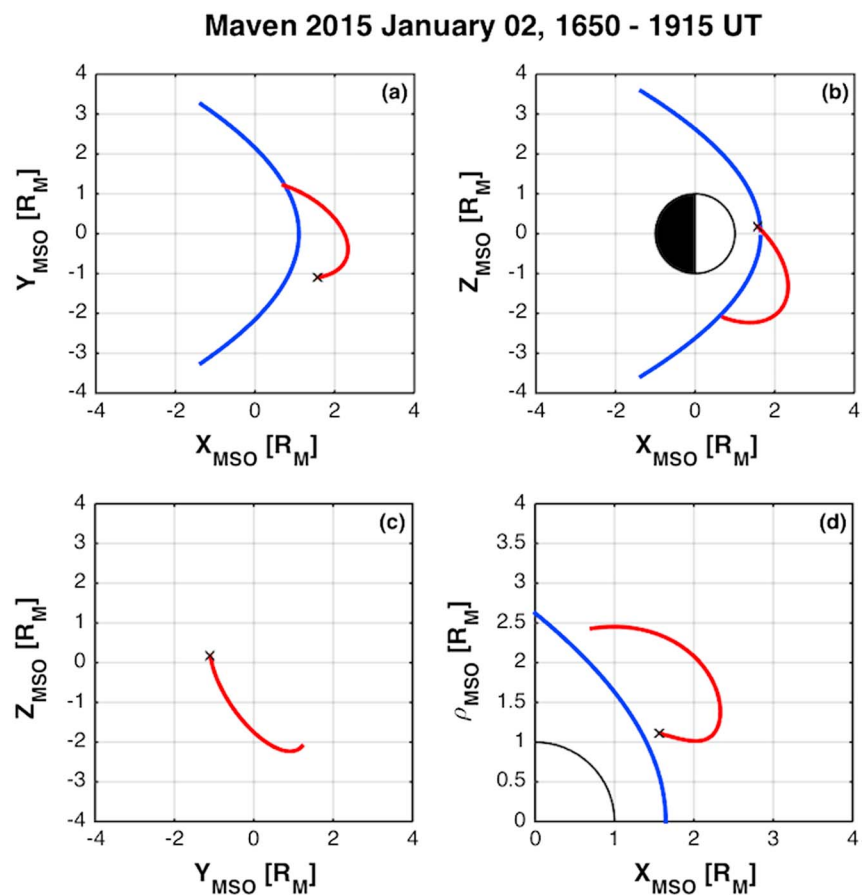


Figure 1. Cross sections of Mars model bow and MAVEN orbiter's path during the time of interest. Mars-centered Solar Orbital (MSO) system of coordinates is used.

during January and February 2015 MAVEN orbits show similar features with the event presented here. During this 2 month period, the spacecraft crossed the bow shock regions near the nose. For this event, the location of the MAVEN spacecraft along its elliptical orbit is shown (in red) in Figure 1. The shape of the Martian bow shock (in blue) is also displayed on the same figure. In this respect and following previous studies, the shock is represented by a conic section whose center is offset from the planet center. Studies of the Mars' bow shock are based on Mars 2, 3, and 5 spacecraft [Russell, 1977; Slavin et al., 1991], Phobos-2 [Schwingenschuh et al., 1990; Slavin et al., 1991; Trotignon et al., 1991], and MGS orbiter [Vignes et al., 2000; Edberg et al., 2008]. All models consist in a fit procedure of crossing locations and are therefore purely mathematical in nature. In this respect, conic sections with fixed parameters are considered; no adjustment for solar wind and magnetic field conditions are introduced as it is usually the case for the Earth bow shock. Our choice of the model reported by Vignes et al. [2000] is dictated by the fact that the fit uses a larger statistic and includes a significant number of crossings far from the nose. The latter model is in a very good agreement with the study of Edberg et al. [2008], which is based on an extensive number of Martian bow shock crossings by MGS. Precisely, the bow shock model in the present study uses the following parameters: eccentricity $\epsilon = 1.03$, semilatus $L = 2.04 R_M$, and an offset position $X_0 = 0.64 R_M$. The fit includes a 4° correction angle due to aberration that results from the Mars orbital motion around the Sun. Bow shock cross sections in the planes $Z = \bar{Z}$ (Figure 1a), $Y = \bar{Y}$ (Figure 1b), and $X = \bar{X}$ (Figure 1c) are shown in black curves; \bar{X} , \bar{Y} , and \bar{Z} are the average Mars Solar Orbital (MSO) coordinates of MAVEN position during the time of interest indicated on the top of Figure 1. Because the planet was out of the planes $X = \bar{X}$ ($\bar{X} = 1.87 R_M$) and $Z = \bar{Z}$ ($\bar{Z} = -1.50 R_M$), it is not shown in Figures 1a and 1c. In addition, Figure 1d provides a view in the cylindrical coordinates frame. MAVEN trajectory is shown in red, and cross indicates the initial time interval. As shown, the spacecraft emerges from an outbound bow shock crossing and heads toward an inbound crossing at the end of the time interval.

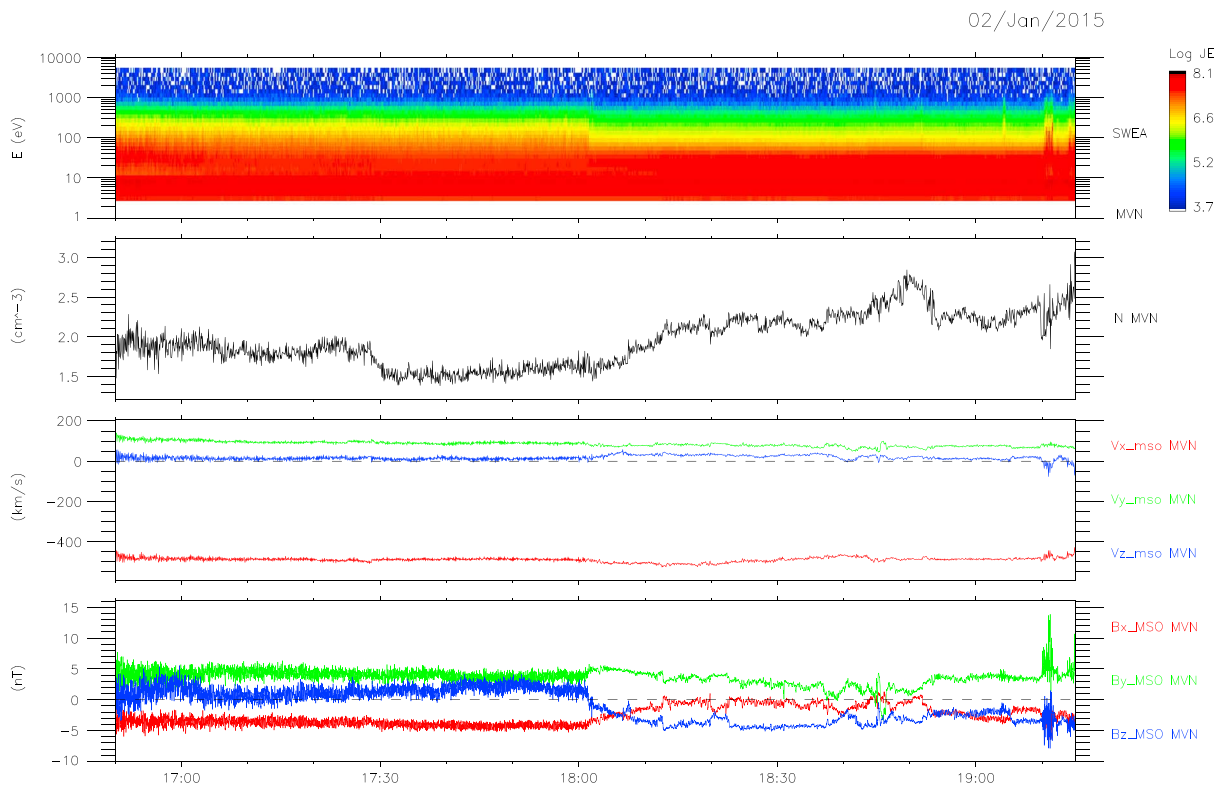


Figure 2. (first panel) The MAVEN-SWEA energy spectrogram for 2 January 2015, 1650–1915 UT. The following successive panels display respectively (second panel) the ion density, (third panel) the MSO components of the solar wind velocity, and (fourth panel) the magnetic field.

The particle and magnetic field measurements are now presented. From top to bottom successive panels of Figure 2 show the SWEA energy spectrogram, the solar wind ion density and velocity from SWIA, and the magnetic field from MAG measurements obtained on 2 January 2015, 1650–1915 UT. The solar wind velocity and magnetic field components are given in MSO coordinates. The event duration corresponds to the elapsed time between an outbound-inbound bow shock crossings occurred at 1630:20 UT and 1916:15 UT, respectively (not shown). At ~1801:40 UT, a clear IMF rotation occurs as indicated in the B_x and B_z components simultaneously accompanied by a significant drop in the energetic electron flux to the solar wind level and in the amplitude of magnetic field temporal fluctuations. Following the IMF rotation, successive flux spikes appear at ~1802:00 UT and ~1904:02 UT. The electron spikes occur only for various energy thresholds. We now examine precisely the causal relation between the magnetic connection of the spacecraft with the shock and the electron flux enhancement. The determination of magnetic connection parameters basically includes the shock normal θ_{Bn} , the distance DIST of the spacecraft from the shock measured along the IMF direction and the foreshock depth DIF, and the distance parallel to the X direction of the spacecraft position from the IMF tangent line. The determination of these parameters is based on the Mars bow shock model as described above [Vignes *et al.*, 2000]. The derivation of connection parameters is easily tractable; however, it is assumed that the ambient magnetic field is uniform during the time of interest and that it is represented by a straight line between the shock and the spacecraft. To reduce the errors, the determination of the ambient field requires the suppression of low-frequency fluctuations which are always present in the foreshock region. A running average of MAG data over several points provides a satisfactory result.

Figure 3 (first panel) shows the time series of the electron flux for eight selected energy ranges as indicated. Figure 3 (second panel) shows the deviation of the instantaneous magnetic field B_x component with respect to an eleven-seconds (11s) running average. The following panels show the angle θ_{Bn} (Figure 3, third panel), the distance DIST (Figure 3, fourth panel), and the foreshock depth DIF (Figure 3, fifth panel), respectively. When the spacecraft is not magnetically connected, there are no numerical values for DIST and θ_{Bn} , and DIF is negative. Figure 3 clearly shows the dependence of the electron flux level with the magnetic connection to the shock. First, enhanced energetic electron flux is no longer present after the occurrence of an IMF rotation

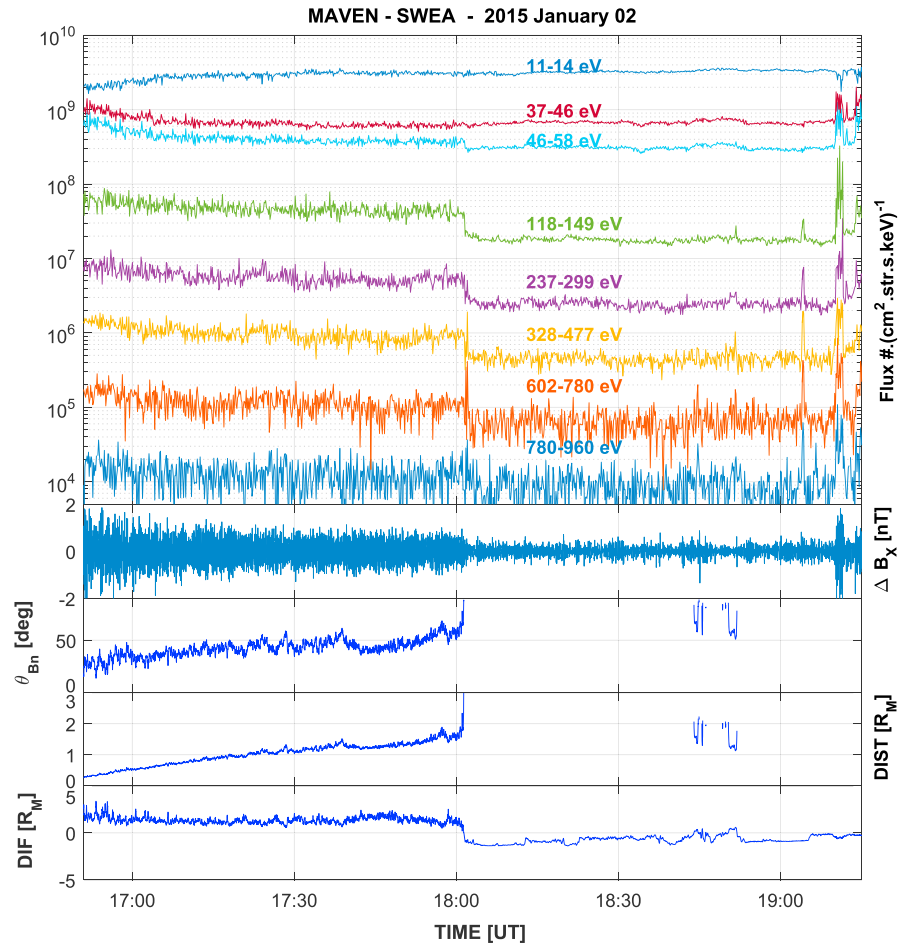


Figure 3. (first panel) The electron flux for eight selected energy ranges, (second panel) the B_x fluctuation level with respect to a running average, (third panel) the angle θ_{Bn} , (fourth panel) the distance of MAVEN to the shock DIST, and (fifth panel) the foreshock depth DIF.

at 1801:40 UT, which is followed by a loss of connection to the shock by MAVEN just prior to the appearance of an electron burst with $E \geq 328$ eV. In addition, the flux line plots given on the top panel show two weak but significant electron bursts at $\sim 1844:45$ UT and $\sim 1851:40$ UT; the first burst is associated with electrons with $E \geq 602$ eV. These two bursts do not appear in the energy spectrogram of Figure 2 because of their low intensity as well as the fact that an interpolation has been performed on the data. The association of the electron flux level with the shock θ_{Bn} angle is emblematic for the Martian electron foreshock. The modest but clearly noticeable monotonic decay in the energetic electron flux level is accompanied by an increase of θ_{Bn} angle from a quasi-parallel configuration to $\theta_{Bn} \sim 90^\circ$ just before the flux drops to the background level. This event clearly demonstrates that the energetic electrons populate the entire foreshock space covered by the MAVEN orbiter. This electron flux θ_{Bn} dependence appears quite remarkable and seems to indicate that the foreshock electrons emanate from the entire Mars bow shock surface. Also, it is not clear whether the perceptible flux decay is due to changing conditions at the shock or resulting from the distance covered by the electrons. Moreover, this trend is simultaneously accompanied by a decay in the magnetic fluctuations during the time where MAVEN is connected to the shock; a similar feature is seen on both the B_y and B_z components (not shown). When related to electrons, this association appears puzzling since the IMF fluctuations basically consist of ultralow-frequency (ULF) waves excited by ubiquitous pickup ions and eventually back-streaming ions [Mazelle et al., 2004]. In addition, the bottom panel clearly indicates that the IMF fluctuations decay with increasing distance from the shock (and therefore the planet) which may suggest that pickup ions are the dominant energy source and consequently may explain the IMF fluctuations decay. Moreover, the successive electron bursts indicated above is another striking feature of Martian foreshock. These bursts appear only above a certain energy threshold. We also notice that Vignes et al. [2000] model bow shock provides

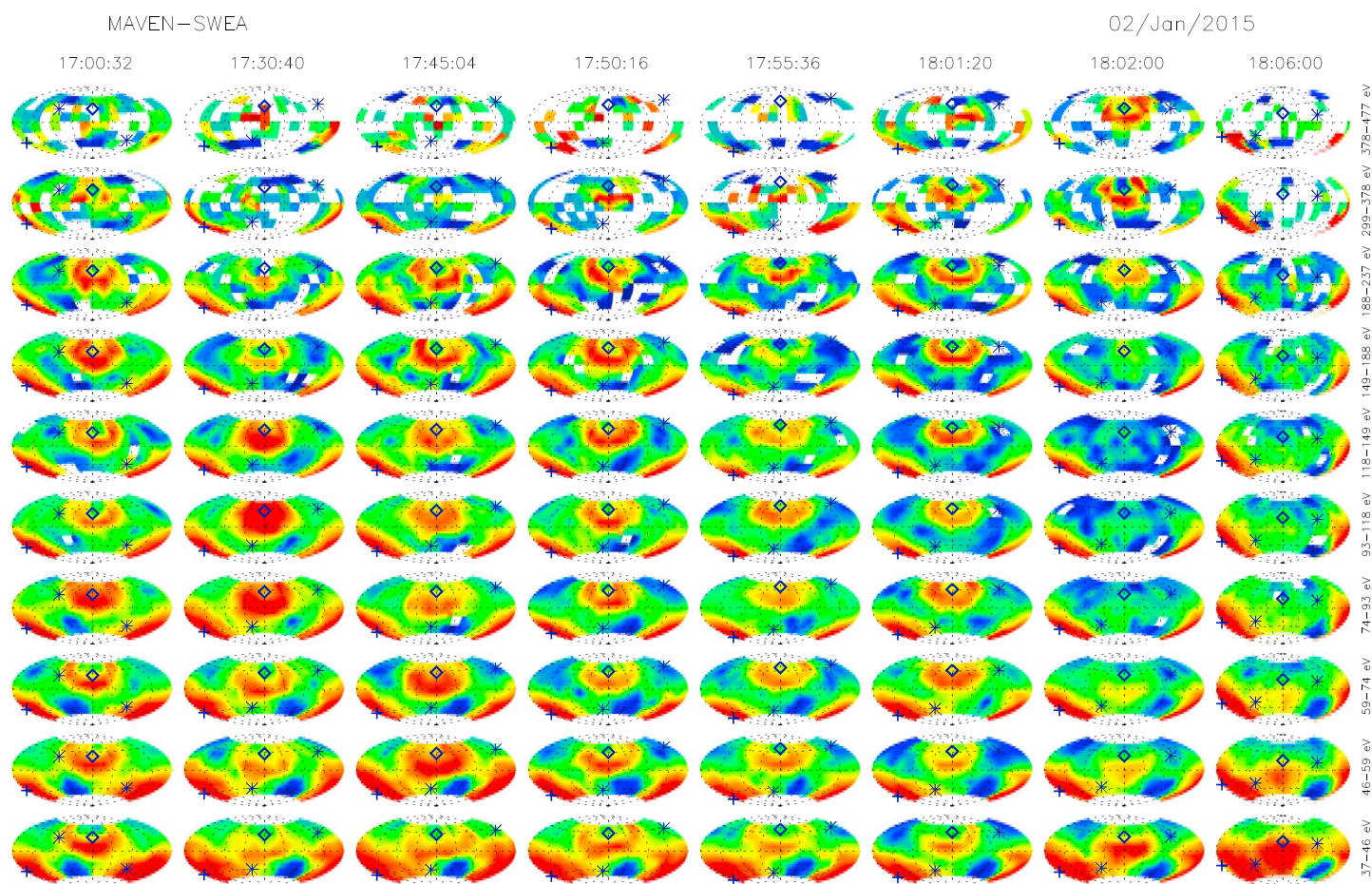


Figure 4. Snapshots of electron angular distribution for 10 selected energy ranges. The Hammer-Aitoff equal area projection is used. The cross (diamond) symbol represents the direction of \mathbf{B} ($-\mathbf{B}$) direction. The color scale corresponds to distribution function values and is normalized for each Hammer-Aitoff slice.

quite satisfactory results for it restores the magnetic connection associated with the electron bursts seen at $\sim 1844:45$ UT and $\sim 1851:40$ UT. Although the $\sim 1904:02$ UT electron burst is not accounted for by the model bow shock, the corresponding foreshock depth is near zero, which indicates that the lack of agreement is due to uncertainties of the model since it has maximum effect near the magnetic field tangent line.

We now examine in detail the electron dynamics. The Hammer-Aitoff equal area projection [Mailing, 1992] is used to represent three-dimensional measurements of electron distributions as shown in Figure 4. The projection is appropriate to display 4π sr projections for a given energy [Larson et al., 1996; Meziane et al., 2001]. Each slice is a representation in pitch angle (radial extent)-gyrophase (polar angle) dimensions for a fixed energy. In this representation, field-aligned propagating particles show a phase space density peak centered on the cross or diamond symbol (indicating the direction of \mathbf{B} or $-\mathbf{B}$, respectively). The blank polar sectors visible in each distribution are velocity space sectors that are not covered by SWEA. Finally, we should mention that Hammer-Aitoff slices of Figure 4 are constructed in the spacecraft reference frame. A judicious representation of the angular distribution would require a transformation into the plasma frame of reference. However, for electron energies $E \geq 70$ eV, the reference frame transformation conveys only small qualitative changes and therefore are not considered here.

During the time interval of interest, the magnetic field direction is planetward, the backstreaming particles are therefore primarily streaming in $-\mathbf{B}$ direction indicated by the diamond symbol as shown on each Hammer-Aitoff slice. Figure 4 shows eight snapshots for 10 energy ranges with numerical values indicated on the figure's right side. The last snapshot (last column) corresponds to the solar wind electron distribution taken at 1806:00 UT when MAVEN was upstream outside the foreshock. In this case, the solar wind strahl (indicated by the cross symbol) forms the dominant component. When the energy decreases below 59 eV, the electron

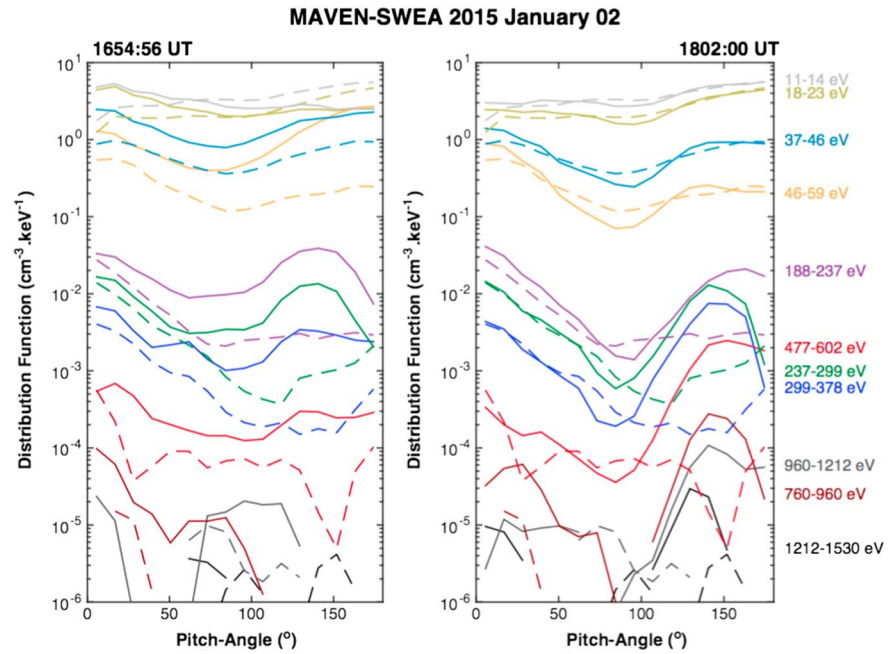


Figure 5. Two snapshots of the electron distribution measured by MAVEN-SWEA instrument. The solar wind distribution is represented by the dashed lines, and the energy ranges are indicated on the right panel. An instant for which the magnetic field direction is connected at a (left) quasi-parallel and (right) quasi-perpendicular geometry.

flux associated with the solar wind halo component is enhanced. The successive snapshots are taken at various times, initially from 1700:32 UT corresponding to a quasi-parallel configuration to a quasi-perpendicular one at 1802:00 UT. Figure 4 depicts several remarkable features. First, the solar wind strahl is always present. Second, a nearly closed ring or annulus centered along $-\mathbf{B}$ direction and representing a peak in phase space density is seen for almost all energies. For quasi-parallel and oblique geometries, the ring in phase space is present for $E \leq 237$ eV only. Higher-energy rings appear only when MAVEN is connected to the foreshock edge, and at the same time $E \leq 237$ eV backstreaming electrons are absent. There is no clear evidence that the radius of the ring (which corresponds to the pitch angle) is energy dependent.

On a quantitative aspect, the angular distribution functions of Figure 4 are integrated over the gyrophase to retrieve a more conventional representation of pitch angle distributions; the latter are now given in the plasma rest frame of reference. Figure 5 shows the distribution recorded at the beginning (left) and end (right) of the interval corresponding to a quasi-parallel (left) and perpendicular (right) geometry. Each continuous curve represents the distribution at a fixed energy, and the dashed curve shows the solar wind as recorded later on at 1806:00 UT when MAVEN is not magnetically connected to the shock. Figure 5 clearly exhibits the solar wind electron halo, an isotropic component of low-energy ($E = 11 - 23$ eV) electrons, and high-energy ($E > 23$ eV) electrons streaming along the magnetic field which corresponds to the strahl. Both components are clearly distinct whether the spacecraft is magnetically connected or not, because measured about 1 h earlier, the solar wind phase space density values shown in the 1654:56 UT panel appear significantly different from the actual values. When the spacecraft becomes connected, a significant flux of electrons streaming sunward above the solar wind level is seen for energies $E > 23$ eV. Clearly, the electron pitch angle distribution exhibits slight quantitative differences, whether it is observed along the IMF lines connecting a quasi-parallel or a quasi-perpendicular shock region. In the former case, where the θ_{Bn} angle is estimated to 20° , the backstreaming electrons have maximum phase space density values for pitch angles $\sim 135^\circ$ except perhaps at energies $E \leq 59$ eV for which the distribution peaks at a lower pitch angle value. At nearly perpendicular shock, only electrons with an energy $E \geq 188$ eV have phase space density values above the solar wind threshold level and significantly higher than those observed for oblique and quasi-parallel geometries. The event appears as a burst in which only electrons with energies higher than 188 eV exhibit a flux enhancement. In this case, the phase space density peaks at higher pitch angle $\sim 140^\circ$ in the 237–1212 eV energy range and at $\sim 160^\circ$ for 188–211 eV electrons. There is an indication that the highest-energy spike observed occurs in the 1212–1530 eV energy channel exhibiting a phase space density peak at $\sim 130^\circ$ pitch angle.

4. Discussion

Prior to proceeding with the interpretation of the results, we believe that is very instructive to draw a parallel with the terrestrial electronic foreshock. For this purpose, we briefly present a summary about what has been reported previously and considered to be the established norm. In the terrestrial electron foreshock, the solar wind forms the core of the ambient plasma in addition to the backstreaming electrons emanating from the shock and moving sunward. The energy range of the latter population spans from 10 eV to up to ~ 100 keV. Using ISEE 1 and 2 data, *Anderson et al.* [1979] reported that the most energetic electrons are spatially organized in sheets with depths that scale with $1/v_{\parallel}$, where v_{\parallel} is the electron parallel velocity. Precisely, the most energetic electrons emanate near the tangent line, whereas less energetic emerge from regions located relatively deeper, inside from the IMF tangent line. The bursty appearance of the most energetic electrons coincides with the IMF line tangent to the bow shock sweeping the spacecraft and therefore defines an unambiguous proxy for a foreshock boundary crossing. Less energetic electrons ($E \leq 1.5$ keV) seem to come from a broad shock surface region. The flux of these electrons is highest near the perpendicular shock and then drops downstream toward the quasi-parallel region. Because of the velocity filtering due to the solar wind electric field convection, the foreshock electrons and ions appear spatially separated.

The observations described above put stringent constraints on physical models explaining the electron energization. Electron acceleration at quasi-perpendicular shocks is a mature topic, and seminal works by *Wu* [1984] and *Leroy and Mangeney* [1984] form the main theoretical framework for the understanding of the acceleration mechanism. Further extended work emphasized on the spectra and angular distributions of the accelerated electrons [*Vandas*, 2001]. These models are based on an adiabatic reflection off the shock of thermal electrons, first developed by *Sonnerup* [1969] seminal work on shock-particle encounter. The basic mathematical framework uses the deHoffman-Teller reference frame to track the charged particle orbit. When transformed back to the laboratory frame, the particle gains energy. The first observational evidence that the IMF tangent line plays a relevant place in electron acceleration was pointed out by *Filbert and Kellogg* [1979]. The theoretical models provide comprehensive resources if any comparison with observations is attempted. Other physical models have also been put forward to account for the production of backstreaming electrons. *Smith* [1971] suggested that downstream electrons are heated through ion acoustic turbulence, allowing the most energetic electrons to escape upstream. In another model, electron acceleration occurs during the nonlinear growth phase of waves excited by ion reflection at quasi-perpendicular shock [*Tanaka and Papadopoulos*, 1983]. Although the reflection model provides a good agreement with the observations, further studies are needed in order to appreciate the relevance of wave heating processes to the production of backstreaming electrons. We, however, emphasize that the reflection model predicts an exponential spectrum, whereas the observed one follows a power law in energy. A strong evidence of the reflection model was first reported by *Feldman et al.* [1983] and later by *Larson et al.* [1996]. Using three-dimensional capability of the Wind/EESA instrument, the latter authors reported for the first time loss cone distributions associated with electrons seen in the terrestrial foreshock along field lines connected to quasi-parallel shock region. Remarkably, the observations show that the loss cone angle decreases with increasing energy indicating the effect of the cross-shock potential on low-energy electrons.

The sudden increase of the electron flux near the IMF tangent line reported in the present study for Mars is likely similar to the thin sheets reported by *Anderson et al.* [1979] for the terrestrial foreshock. Despite the striking differences in the shock structure of Earth and Mars, it seems that the same physical mechanism is operating at the respective foreshock edges, that is, a mirror reflection of a portion of solar wind electrons. The process is supported by the salient features seen in the electron pitch angle distributions. Given the loss cone angular distributions seen above, the magnetic mirroring appears the most appealing physical model to account for the observations. Based on the Martian bow shock model described above, the distribution seen at the foreshock edge at 1802:UT coincides with an IMF line, making an angle of $\theta_{Bn} \sim 87^\circ$ which corresponds to a shock speed $V_s \sim 8.6 \times 10^3$ km s⁻¹. It results that only electrons with energy greater than $E_s \sim 200$ eV can escape upstream. This result is in a very good agreement with the observations shown in Figure 5. Pursuing the investigation further, the loss cone angle energy dependence seen above provides essential elements to compare with the mirror reflection hypothesis. In the plasma rest frame of reference, a mirror-reflected particle distribution peaks at a pitch angle α_c that is given by [*Decker*, 1983]

$$\mu_c = \cos \alpha_c = \frac{1}{N} \left(\eta + \sqrt{(N-1)(N-\eta^2)} \right) \quad (1)$$

where N is the shock magnetic jump and $\eta^2 = E_s/E$; the energy E_s is related to the shock speed, whereas E is the particle energy. Upstream escaping particles should be faster than the shock speed ($\eta \leq 1$). Differentiating equation (1) with respect to η , we can derive the pitch angle difference of two particles escaping upstream with energies E_1 and E_2 :

$$\Delta\alpha_c = \int_{\eta_1}^{\eta_2} \frac{d\eta}{N\sqrt{1-\mu_c^2}} \left(1 - \eta\sqrt{\frac{N-1}{N-\eta^2}} \right) \quad (2)$$

The formula (2) is tested for the 1802:00 UT electron burst, and the choice of $E_s \sim 200$ eV is justified. The shock magnetic field jump is a free parameter, and as shown below, the exact value of N is not determinant given the limited SWEA angular resolution. Let us take $E_1 = 960\text{--}1212$ eV which corresponds to the highest-energy channel that exhibits a significant flux for the 1802:00 UT burst. With respect to the latter energy channels, particles with energies $E_2 = 760\text{--}960$ eV, $E_2 = 477\text{--}602$ eV, $E_2 = 299\text{--}378$ eV, $E_2 = 237\text{--}299$ eV, and $E_2 = 188\text{--}211$ eV have pitch angle smaller by 1.7° , 6.2° , 12.0° , 15.6° , and 19.1° , respectively, for $N = 3$. A higher (lower) value of N will reduce (increase) the predicted cone angle by $2^\circ\text{--}3^\circ$. As a result, the $E_2 = 188\text{--}211$ eV is the only energy channel that can show a sufficient pitch angle difference resolved by SWEA. The predicted pitch angle difference (19.7°) is in very good agreement with the observations (20°).

The mirror reflection picture described above provides a simple mathematical frame to determine closed forms for the energization and angular distribution of the foreshock electrons. Actually, the underlying physics is related to electrons drifting along the shock surface accelerated by the solar wind electric field. The electrons leave the shock when they acquire enough energy to escape upstream. In such a process, it would be instructive to estimate the energization ratio for a particle drifting along the terrestrial bow shock in comparison to that of Mars. For this purpose, we use a heuristic approach, and for simplicity, we consider a perpendicular shock. The energy increase of a particle drifting a distance s along the shock surface accelerated by the tangential convective electric field is given by

$$\Delta E = eVB \sin \phi \times s \quad (3)$$

where V and B are the solar wind speed and magnetic field, respectively, ϕ is the cone angle, and e is the electron charge. To estimate the distance s , we adopt a paraboloid cross section for the model shock. Given that the cone angle is known, it is straightforward to show that the IMF tangent line intercepts the shock at a distance ρ_T from the X axis given by

$$\rho_T = \frac{1}{2b_s \tan \phi} \quad (4)$$

where b_s is the flaring parameter of the paraboloid defined as the inverse of the distance from the planet center to the shock at $X = 0$. Ideally, the particle drifts on the shock surface along a path s that is proportional to ρ_T . We then deduce an estimate for the particle drift energization ratio q , comparing the case for Earth's bow shock to that of Mars:

$$q \sim \frac{B_E \cos \phi_E}{B_M \cos \phi_M} \frac{b_{sM}}{b_{sE}} \quad (5)$$

where E (M) refers to Earth (Mars). To obtain expression (5), the solar wind speed is assumed the same at 1 AU and 1.5 AU. To estimate the factor q , we consider the following nominal values. Based on the Parker spiral of the IMF, $\phi_E \sim 45^\circ$ and $\phi_M \sim 57^\circ$. Also, bow shock statistical models provide $b_{sE} \sim 0.0223 R_E^{-1}$ (R_E Earth radius) and $b_{sM} \sim 0.25 R_M^{-1}$. Finally, $B_E \sim 2.25 B_M$. Using these nominal values, we find $q \sim 60$. Terrestrial electrons have been reported with a maximum energy ~ 100 keV seen at the edge of the foreshock. This derivation indicates that for Mars, the upper threshold of the electron energization is below ~ 2 keV, in a very good agreement with the observations reported in the present work.

A remarkable distinct feature appears in the Martian electron foreshock that is not essentially seen in the case of Earth's foreshock. Electron flux enhancement always occurs when the spacecraft is magnetically connected to the Martian bow shock. It results that energetic electron flux enhancements provide a reliable and an unambiguous proxy of the spacecraft magnetic connection. In the case of the terrestrial foreshock, this proxy role is carried by ions except near-perpendicular connection. In substance, the electron source region is the entire Martian shock surface. No less important, the highest electron fluxes are seen for a quasi-parallel

geometry to moderately decay with increasing θ_{Bn} angle, which contrasts with the terrestrial electron foreshock. The decay of electron flux with increasing θ_{Bn} is not accounted by an adiabatic reflection model, and it seems that the role of the cross-shock potential is not appreciable based on the signature seen in the pitch angle distributions. However, this important point needs more scrutiny before it is confirmed. In the case of the terrestrial bow shock, the presence of a significant cross-shock potential pulls low-energy electrons downstream toward the magnetosheath. This effect has been reported by Larson *et al.* [1996] for foreshock electrons observed on IMF lines connecting the quasi-parallel Earth's bow shock. In contrast, there is no observational evidence that a similar effect is operating at the Mars bow shock as indicated by the pitch angle distributions. This particularity reflects a fundamental difference in the shock structure between Earth and Mars. Alternatively, the observations may suggest that the distance from the shock could be a significant parameter that may account for the electron flux decay. However, it seems to be unlikely, given that the electron diffusion occurs on length scales that are beyond MAVEN orbit.

5. Conclusion

MAVEN orbiter provides a substantial coverage of the region upstream of the Mars bow shock providing an excellent opportunity for planetary foreshock studies. Significant flux enhancements above the solar wind threshold of energetic electrons streaming sunward simultaneously occurs when MAVEN orbiter is magnetically connected to the Martian bow shock. Observational evidences indicate that two types of foreshock electrons are present:

1. The electron spikes with maximum energy $E_{\max} \sim 2$ keV produced at the foreshock boundary and are similar to their counterpart observed at Earth under similar conditions. Fast-Fermi process seems to be the main physical mechanism producing these spikes.
2. A second population that originates from the entire Martian bow shock surface with a decreasing flux level for increasing shock θ_{Bn} values. Although the observed pitch angle distributions seem to indicate that a reflection process is taking place at the shock surface, the θ_{Bn} dependence of the flux needs to be understood.

Acknowledgments

MAVEN data are publicly available through the Planetary Data System. K.M. thanks Emmanuel Penou for his devotion in providing his valuable help in CL software development tool. K.M. wishes to express his thanks to the IRAP in Toulouse for the support in the collaboration work on MAVEN. C.M. and K.M. thank CNES for its support for the part of this work based on the observations with the SWEA instrument on board MAVEN. Work at UNB is supported by the Canadian Natural Science and Engineering Council. K.M. thanks both referees for their valuable comments.

References

- Acuña, M. H., et al. (1998), Magnetic field and plasma observations at Mars: Initial results of the Mars Global Surveyor mission, *Science*, *279*, 1676–1680.
- Anderson, K. A., R. P. Lin, F. Martel, C. S. Lin, G. K. Parks, and H. Rème (1979), Thin sheets of energetic electrons upstream from the Earth's bow shock, *Geophys. Res. Lett.*, *6*, 401–404.
- Axford, W. I. (1962), The interaction between the solar wind and the Earth's magnetosphere, *J. Geophys. Res.*, *67*, 3791–3796, doi:10.1029/JZ067i010p03791.
- Chaffin, M. S., et al. (2015), Three-dimensional structure in the Mars H corona revealed by IUVS on MAVEN, *Geophys. Res. Lett.*, *42*, 9001–9008, doi:10.1002/2015GL065287.
- Connerney, J. E. P., J. Espley, P. Lawton, S. Murphy, J. Odum, R. Oliverson, and D. Sheppard (2015), The MAVEN magnetic field investigation, *Space Sci. Rev.*, *195*, 257–291, doi:10.1007/s11214-015-0169-4.
- Decker, R. B. (1983), Formation of shock-spike events at quasi-perpendicular shocks, *J. Geophys. Res.*, *88*, 9959–9973, doi:10.1029/JA088iA12p09959.
- Edberg, N. J. T., M. Lester, S. W. H. Cowley, and A. I. Eriksson (2008), Statistical analysis of the location of the Martian magnetic pileup boundary and bow shock and the influence of crustal field, *J. Geophys. Res.*, *113*, A08206, doi:10.1029/2008JA013096.
- Feldman, C. W., et al. (1983), Electron velocity distributions near the Earth's bow shock, *J. Geophys. Res.*, *88*, 96–110.
- Filbert, P. C., and P. J. Kellogg (1979), Electrostatic noise at the plasma frequency beyond the Earth's bow shock, *J. Geophys. Res.*, *84*, 1369–1981, doi:10.1029/JA084iA04p01369.
- Halekas, J. S., E. R. Taylor, G. Dalton, G. Johnson, D. W. Curtis, J. P. McFadden, D. L. Mitchell, R. P. Lin, and B. M. Jakosky (2015), *The solar wind ion analyzer for MAVEN*, vol. 195, 125–151.
- Jakosky, B. M., et al. (2015a), The MAVEN mission to Mars, *Space Sci. Rev.*, *195*, 3–48, doi:10.1007/s11214-015-0139-x.
- Jakosky, B. M., J. M. Grebowsky, J. G. Luhmann, and D. A. Brain (2015b), Initial results from the MAVEN mission to Mars, *Geophys. Res. Lett.*, *42*, 8791–8802, doi:10.1002/2015GL065271.
- Kellogg, P. J. (1962), Flow of plasma around the Earth, *J. Geophys. Res.*, *62*, 3805–3811, doi:10.1029/JZ062i010p03805.
- Kiraly, P., et al. (1991), The HARP plasma experiment on-board the Phobos-2 spacecraft: Preliminary results, *Planet. Space Sci.*, *39*(1/2), 139–145.
- Larson, D. E., et al. (1996), Probing the Earth's bow shock with upstream electrons, *Geophys. Res. Lett.*, *23*(17), 2203–2206.
- Leroy, M. M., and A. Mangeney (1984), A theory of energization of solar wind electrons by the Earth's bow shock, *Ann. Geophys.*, *2*, 449–456.
- Mailing, D. H. (1992), *Coordinate Systems and Map Projections*, 2nd ed., Pergamon Press, New York.
- Mazelle, C. X., et al. (2004), Bow shock and foreshock phenomena at Mars, *Space Sci. Rev.*, *111*, 115–181.
- Meziane, K., C. X. Mazelle, R. P. Lin, D. LeQuéau, D. E. Larson, G. K. Parks, and R. P. Lepping (2001), Three-dimensional observations of gyrating ion distributions far upstream from the Earth's bow shock and their association with low-frequency waves, *J. Geophys. Res.*, *106*, 5731–5742, doi:10.1029/2000JA900079.
- Mitchell, D. L., et al. (2015), The MAVEN Solar Wind Electron Analyzer, *Space Sci. Rev.*, *200*, 495, doi:10.1007/s11214-015-0232-1.
- Russell, C. T. (1977), On the relative locations of the bow shocks of the terrestrial planets, *Geophys. Res. Lett.*, *4*, 387–390.

- Schwingschuh, K., W. Riedler, H. Lichtenegger, Ye. Yeroshenko, K. Sauer, J. G. Luhmann, M. Ong, and C. T. Russell (1990), Martian bow shock: Phobos observations, *Geophys. Res. Lett.*, *17*, 889–892.
- Skalsky, A., R. Gard, P. Kiraly, S. Klimov, V. Kopanyi, K. Schwingschuh, and J. G. Trotignon (1993), Simultaneous plasma wave and electron flux observations upstream of the Martian bow shock, *Planet. Space Sci.*, *3*, 183–188.
- Slavin, J. A., K. Schwingschuh, W. Riedler, and E. Eroshenko (1991), The solar wind interaction with Mars: Mariner 4, Mars 2, Mars 3, Mars 5 and Phobos 2 observations of bow shock position and shape, *J. Geophys. Res.*, *96*, 11,235–11,241.
- Smith, D. F. (1971), Plasma radiation from collisionless MHD shock waves: 1. Shock region analysis, *Astrophys. J.*, *170*, 559.
- Sonnerup, B. U. Ö. (1969), Acceleration of particles reflected at the shock front, *J. Geophys. Res.*, 1301–1304, doi:10.1029/JA074i005p01301.
- Tanaka, M., and K. Papadopoulos (1983), Creation of high-energy electron tails by means of the modified two-stream instability, *Phys. Fluids*, *26*, 1697–1699.
- Trotignon, J. G., R. Gard, and S. Klimov (1991), Location of the Martian bow shock measurements by the plasma wave system on Phobos-2, *Geophys. Res. Lett.*, *18*(3), 365–368.
- Vandas, M. (2001), Shock drift acceleration of electrons: A parametric study, *J. Geophys. Res.*, *106*, 1859–1871.
- Vignes, D., C. X. Mazelle, H. Rème, M. H. Acuña, J. E. P. Connerney, R. P. Lin, D. L. Mitchell, P. Cloutier, D. H. Crider, and N. F. Ness (2000), The solar wind interaction with Mars: Locations and shapes of the bow shock and the magnetic pile-up boundary from the observations of the MAG/ER experiment onboard Mars Global Surveyor, *Geophys. Res. Lett.*, *27*(1), 49–52.
- Wu, C. S. (1984), A fast Fermi process: Energetic electrons accelerated by a nearly perpendicular bow shock, *J. Geophys. Res.*, *89*, 8857–8862.